Dynamics of spray and swirling flame under acoustic oscillations: A joint experimental and LES investigation

Guillaume Vignat, Ermanno Lo Schiavo, Davide Laera, Antoine Renaud, Laurent Gicquel, D. Durox, Sébastien Candel

Version of Record: https://www.sciencedirect.com/science/article/pii/S1540748920301024
Manuscript_9b0c2087901b35579bace625104670bb

Dynamics of Spray and Swirling Flame under Acoustic Oscillations : A Joint Experimental and LES Investigation

Guillaume Vignat[a,*], Ermanno Lo Schiavo[b], Davide Laera[b], Antoine Renaud[a], Laurent Gicquel[b], Daniel Durox[a], Sébastien Candel[a]

[a] *Laboratoire EM2C, CNRS, CentraleSupélec, Université Paris-Saclay, 3 rue Joliot Curie, 91192 Gif-sur-Yvette, France*
[b] *CERFACS, 42 avenue Gaspard Coriolis, 31057 Toulouse, France*

Abstract

The dynamics of spray swirling flames is investigated by combining experiments on a single sector generic combustor and large eddy simulations of the same configuration. Measurements and calculations correspond to a self-sustained limit cycle operation where combustion coupled by an axial quarter wave acoustic mode induces large amplitude oscillations of pressure in the system. A detailed analysis of the mechanisms controlling the process is carried out first by comparing the measured and calculated spray and flame dynamics. Considering in a second stage that the spray and flame are compact with respect to the acoustic wavelength the analysis can be simplified by defining state variables that are obtained by taking averages over the combustor cross section and representing the behavior of these average quantities as a function of the axial coordinate and time. This reveals a first region in which essentially convective processes prevail. The convective

*Corresponding author:
Email address: guillaume.vignat@centralesupelec.fr (Guillaume Vignat)

heat release rate then couples further downstream with the pressure field giving rise to positive Rayleigh source terms which feed energy in the axial acoustic mode. In the convective region, the swirl number features oscillations around its mean value with an impact on the flow aerodynamics and flame radial displacement. Fluctuations in the fuel flow rate are initiated at the injector exhaust and likewise convected downstream. The total mass flow rate that exhibits strong convective disturbances is dominated further downstream by the acoustic motion. This information provides new insights on the convective-acoustic coupling that controls the heat release rate disturbances and reveals the time delays governing the combustion oscillation process.
Keywords:
Spray flames; Swirling flames; Combustion instabilities; Large Eddy Simulation; Time delay

---

Colloquium: Gas turbine and rocket combustion

Length of the paper determined using Method 2. Total length of the paper: less than 8 pages

The authors will pay color reproduction charges if applicable.

1. Introduction

Combustion instabilities have many undesirable consequences in terms of life duration and operability and are a source of risk in high performance systems like jet engines or industrial gas turbines [1, 2]. Their prediction,

control and reduction require an understanding of the flame dynamics and the coupling with the resonant modes of the combustion system. Experiments, even well conducted and instrumented [2–4], do not give access to all necessary variables. Large Eddy Simulation (LES) can be used in high fidelity calculations of combustion oscillations in engine like configurations [5, 6].

It is at this point worth briefly reviewing progress made in the simulation of spray flame dynamics under acoustic coupling or under acoustic forcing. Much of the numerical modeling effort has been carried out so far with unsteady RANS calculations [7, 8]. General trends are captured but mismatch with experimental data are also noted. Recent articles, among others [9, 10] report LES results for gas turbine model combustors powered by swirled spray flames with detailed validations with experimental data for the mean variables, but the flame dynamics is not investigated. Tachibana et al. [6] use LES to simulate a spray swirled flame at elevated pressure under self-sustained instability, and observe a good overall agreement with experimental data. They note the importance of the time delay introduced by droplet evaporation on the combustion instability coupling, an effect also described in [11] from LES of the reactive flow in a backward facing step configuration. Eckstein et al. [2] indicate that in air assisted atomization systems, droplet diameter fluctuation will ensue from velocity fluctuations within the injector. These fluctuations create unsteadiness in the fuel supply to the flame and contribute to the instability.

The present investigation focuses on flame dynamics in the swirl spray atmospheric single sector combustor SICCA-Spray. This device features strong

longitudinal oscillations in a limit cycle regime at a frequency (474 Hz) close to that of oscillations in the annular combustor MICCA-Spray [12]. Experiments and LES are combined to contribute to the validation of LES of swirl spray flame dynamics under acoustic interaction, and extract informations on the fundamental mechanisms of flame dynamics. The essence of this analysis is to consider that the flame is compact with respect to the acoustic wavelength. The multidimensional complexity of the problem may then be reduced but it is important to retain the capacity to describe the convective motion in the combustion region and to examine its coupling with the acoustic motion. This may be accomplished by considering variables that are integrated over the combustor cross section. In practice, it is more convenient to use variables that are integrated over an elementary volume $V = S_c \Delta z$ having as a base the combustor cross section S_c and extending over a small Δz in the axial direction:

$$\widehat{\psi}(z,t) = \int_z^{z+\Delta z} \int_{S_c} \psi(r,\theta,z,t)\, dV \tag{1}$$

where r, θ, z are the radial, tangential and axial coordinates. In what follows $\Delta z = 1\,\text{mm}$. It is also sometimes more physical to use variables integrated over the cross section for example when one considers mass flow rates. Such variables will appear as $\widetilde{\psi}$. It is known that combustion instabilities arise when the delay resulting from injection, convection, vaporization and chemical conversion is of the order of a multiple or half multiple of the acoustic period [13]. The variables associated with these processes are perturbed in cascade during the oscillation, and end up creating heat release rate fluctuations which drive the combustion instability. The flame delay mostly results

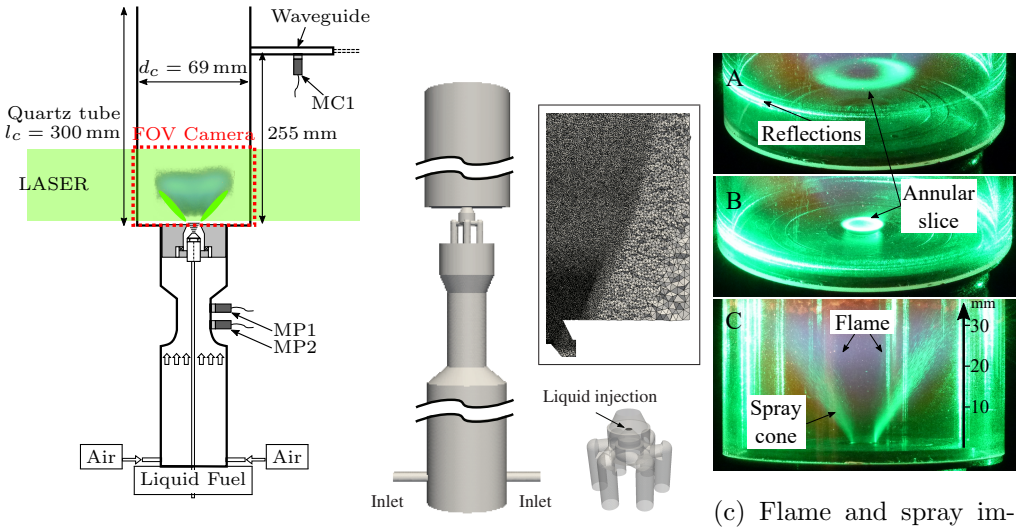

(a) SICCA-Spray test rig. (b) LES domain and mesh. (c) Flame and spray images.

Figure 1: **(a)**: Schematic view of SICCA-Spray. The green plane depicts the laser sheet used for spray tomography. The field of view (FOV) of the camera is indicated by a red contour. **(b)**: Numerical domain and mesh in the flame region. **(c)**: Color image with flame (blue) and spray laser tomography (green) showing the position of the flame with regards to the hollow cone spray. Adapted from [14].

from the longitudinal phase velocity of these perturbations. The space-time analysis based on the integrated variables defined previously allows to identify these perturbations and their velocity.

2. Experimental and Numerical Setup

The experimental configuration SICCA-Spray shown schematically in Fig. 1(a), is an atmospheric single sector test rig designed for combustion dynamics experiments with swirl spray injectors. It comprises a cylindrical plenum equipped with two Bruel & Kjaer type 4938 microphones with type 2670 preamplifier for acoustic pressure and velocity measurements upstream of

the injector. The radial swirler design features a swirl number of 0.63 [12]. Liquid n-heptane is injected by a simplex fuel atomizer creating a hollow cone shaped spray on the centerline. The mean droplet diameter is $d_{10} = 8\,\mu m$ and the Sauter mean diameter $d_{32} = 30\,\mu m$ [12]. The combustion chamber is a cylindrical quartz tube with a microphone "MC1" mounted on a watercooled waveguide at $z_{MC1} = 255\,mm$ above the backplane. The waveguide creates a $640\,\mu s$ delay that is compensated to retrieve the pressure signal in the chamber. The burner is operated at a global equivalence ratio of $\phi_{nom} = 0.85$ and a thermal power of $\mathcal{P} = 6.4\,kW$, corresponding to an air flow rate of $\dot{m}_{air,nom} = 2.58\,g\,s^{-1}$ (measured by a Bronkhorst EL-Flow) and a fuel flow rate of $\dot{m}_{fuel,nom} = 520\,g\,h^{-1}$ (monitored by a Bronkhorst CORI-Flow). A continuous $532\,nm$ $0.5\,W$ laser is used to generate a laser sheet for tomographic visualization of the liquid spray. The laser sheet is orthogonal to the backplane of the combustor and passes through the centerline. A high speed color camera (Phantom V2512) is used for simultaneous visualization of the droplet light scattering (green) and flame chemiluminescence (blue). The camera is operated at a frame rate of $10\,kHz$.

LES of this configuration is performed using the AVBP solver with the modeling strategy of [10]. A third order accurate in time and space Taylor-Galerkin scheme (TTGC) is used along with non-reflecting Navier-Stokes Characteristic Boundary Conditions imposing an atmospheric pressure on the far-field outlet. The SIGMA subgrid scale model is used [15]. A Lagrangian framework is adopted for the liquid spray description by injecting fuel droplets using the FIM-UR model with a constant mass flow rate and distribution (Rosin-Rammler). The droplet-wall interaction inside the injector

is modeled using a film approach [16]. No model is used for inter-particle interaction as the smallest inter-particle distance exceeds 10 droplet diameters shortly downstream of the injector outlet ($z > 5\,\mathrm{mm}$). Particle interaction with subgrid scale eddies is also neglected as the subgrid scale Stokes number $\mathrm{St_{SGS}}$ [17] is estimated to be of the order of 3×10^3. The chemistry is described with the global two-step 6-species scheme $2S\_C_7H_{16}\_DP$ with Pre-Exponential Adjustment (PEA) for rich mixtures [18]. The mesh comprises approximately 20 million tetrahedra with refinement up to $\Delta x \simeq 150\,\mu\mathrm{m}$ at the flame root and $\Delta x \simeq 200 - 300\,\mu\mathrm{m}$ further downstream. As the typical flame thickness is $\delta_{l,\phi=1} = 410\,\mu\mathrm{m}$, dynamic flame thickening (TP-TFLES) is used depending on the local equivalence ratio and only in the premixed regime identified by positive Takeno index values. The evaporation term is also thickened as recommended in [18]. The quality of the LES is evaluated by considering the ratio of turbulent to laminar viscosity, which at maximum and very locally reaches 50. After convergence, a physical time of 43 ms (20 cycles) was simulated under steady oscillations to acquire statistics at a sampling rate of 9.4 kHz.

3. Data Processing for LES Validation

Experimentally, the frequency of the oscillation obtained from the power spectral density (PSD) of the acoustic pressure p'_{MC1} measured by the chamber microphone is $(474 \pm 19)\,\mathrm{Hz}$ (where the uncertainty is evaluated as sum of width at half height and frequency resolution), for an amplitude of 768 Pa (RMS). At the same position, the LES results show that the pressure oscillation reaches 618 Pa (RMS) for a frequency of $(461 \pm 42)\,\mathrm{Hz}$. The focus of the

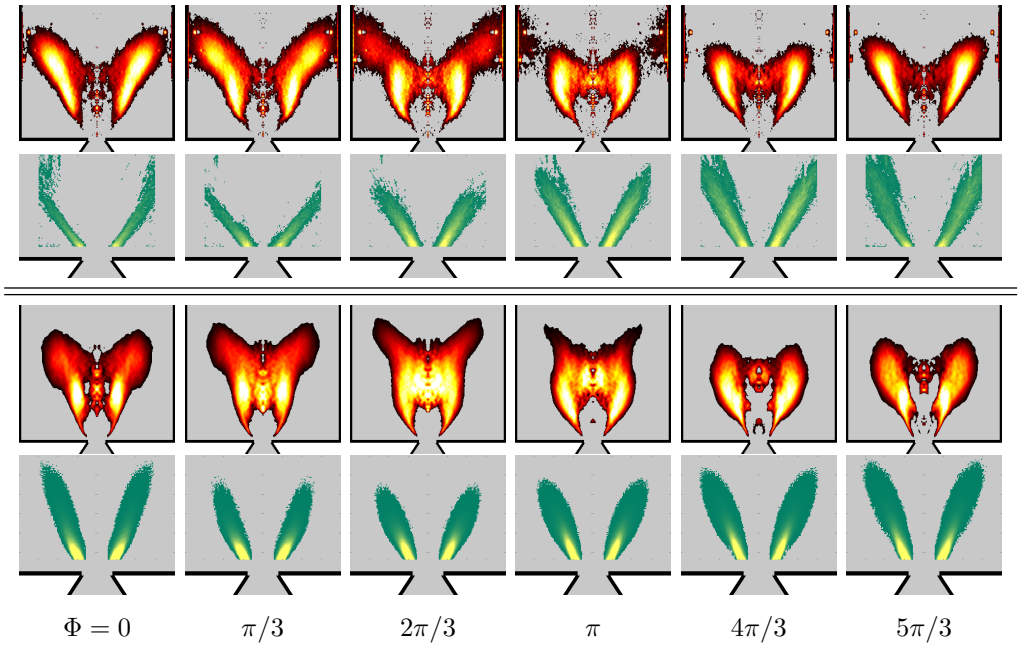

Figure 2: Top: experimental phase averaged chemiluminescence and spray tomography (Mie scattering) images. Bottom: LES phase averaged images of heat release rate, and spray liquid volume fraction multiplied by liquid density $\rho_l \alpha_l$. Spray images are zoomed in. The common reference for the phase is the acoustic pressure signal at microphone MC1.

present section is now placed on the validation of flame and spray dynamics.

The number of cycles that can be simulated is not very large and will not provide statistically well converged phase averages. It is then more appropriate to use the Dynamic Mode Decomposition (DMD) [19] to extract this kind of information. Using this method, and a 200 ms sequence of high speed camera images, it was found that a converged mode shape could be obtained from as little as 20 oscillation cycles, with less than 5% variation in frequency and no visible differences in the spatial structure. This powerful method is used to plot the images shown in Fig. 2. The same processing sequence is applied to the numerical and experimental data. In the experiment, the line of sight integrated chemiluminescence signal recorded by the blue channel on the camera mainly corresponds to emission from excited CH^* radicals within the flame, and may be assumed to be a qualitative indicator of heat release rate. In the simulation, the heat release rate is integrated over the line of sight before DMD is performed. Pseudo-phase averaged images are reconstructed from the 0 Hz and 461 Hz modes. This latter mode corresponds to the thermoacoustic oscillation and dominates the spectrum. These images are then Abel transformed. The phase reference is set by the pressure signal using the snapshot method. Care is taken to keep the same signal duration in the processing of LES and of experimental data. The common DMD processing ensures that no bias is introduced in comparing numerical results and experimental data. The flame exhibits a classical "M" shape. The agreement between LES and experiments is relatively good, although the flame appears to be slightly more opened and a bit longer in the experiment. During the cycle, one observes very little motion at the flame root. A small phase differ-

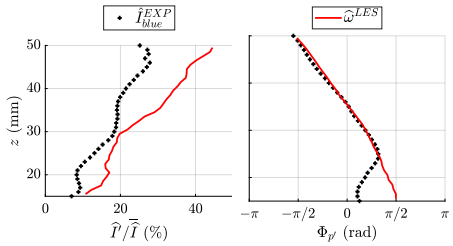

Figure 3: Validation of flame dynamics. From the experiment (black), chemiluminescence signal. From LES (red), heat release rate. Left: axial evolution of the relative amplitude. Right: axial evolution of the phase with respect to acoustic pressure.

ence can be observed between LES and experiment. The bulk of the flame motion happens at the tip of the flame and is reminiscent of that executed by laminar "M" flames responding to incident velocity perturbations [20]: a toroidal structure periodically forms at the tip, separates from the main flame while the fresh reactants enclosed by the toroidal flame surface are rapidly converted into products producing a heat release pulse. This process is observable in the experimental images, for example one observes the decay of the toroidal flame structure between $\Phi = \pi/3$ and $2\pi/3$. Pseudo-phase average spray quantities are also shown in green in Fig. 2. The experimental data corresponding to Mie scattering from the fuel droplets features oscillations in angle and in intensity that are most visible in the vicinity of the injector. Similar features can be observed in the LES results although to a lesser extent. The liquid density scaled by liquid volume fraction $\rho_l \alpha_l$ is shown as it is more physically meaningful. In coherence with the flame shape, the angle of the spray also appears to be slightly under predicted.

To obtain a more quantitative view of flame dynamics, it is interesting as indicated in the introduction to consider variables integrated over a small

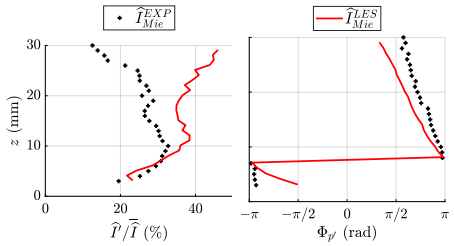

Figure 4: Validation of spray dynamics. Black: experimental Mie scattering on droplets. Red: reconstructed Mie scattering from LES.

cross-section of thickness $\Delta z = 1\,\text{mm}$ ($\widehat{\psi}$, Eq. (1)). Figure 3 depicts heat release rate relative fluctuations from LES and relative intensity fluctuations of light emission by CH* radicals captured by the high speed camera. The phase with respect to pressure is well captured by the LES. The relative amplitude fluctuations are in fair agreement. To examine the spray dynamics in Fig. 4, a pseudo Mie scattering signal is estimated from the discrete lagrangian particles in the LES. Downstream of $z = 25\,\text{mm}$ the experimental signal is affected by reflections of the laser sheet. Again, LES and experiment do not perfectly agree. One cannot expect to match the amplitudes, but the phase evolution is retrieved and the phase velocity of the spray disturbances is only slightly underestimated in the LES.

The validation with experiments is important in order to give weight to the findings from the LES. In this article, the phase and space resolved comparison of the dynamics of the spray and flame in the simulation and in the experiment goes much further than what is found in previous studies dealing with similar issues [6–8, 11]. It is first found that phase average chemiluminescence patterns agree well with the phase averaged heat release rate distributions. While the agreement is not perfect, it is acceptable (Fig.

2). The experimental and LES spray patterns are somewhat different but one could not expect a perfect match. The axial extent of the spray is suitably retrieved but there is a difference in the angular behavior. In the experiment the spray angle opens during the first two phases while this is not retrieved in the simulation. This weakness of the modeling indicates that further improvements are needed in this respect, requiring a better description of the injector near field. For the driving variables of combustion dynamics namely the heat release rate distribution and pressure, a good agreement is obtained between experiments and calculations (Fig. 3). Again, the agreement is not perfect but it is acceptable. The experimental light scattering from the spray is compared with a signal reconstructed from the LES by multiplying the number density by the mean droplet diameter squared to mimic the Mie scattering process. Even for the spray dynamics the amplitudes differ but the agreement is adequate in terms of phase (Fig. 4). Thus, the calculations retrieve many dynamical features to a reasonable degree allowing to deploy the methodology exposed in the next section. Some additional analysis and validation of the present modeling strategy for LES can be found in [21].

4. Analysis of the driving mechanisms

The focus is now placed on the detailed analysis of the LES. Throughout this section, a space-time representation is used in which time t and position z are horizontal and vertical coordinates respectively. Variables are integrated over the elementary volume V or over the cross section S_c as defined previously ($\widehat{\psi}$ and $\widetilde{\psi}$ respectively, Eq. (1)). It is first interesting to consider the Rayleigh source term:

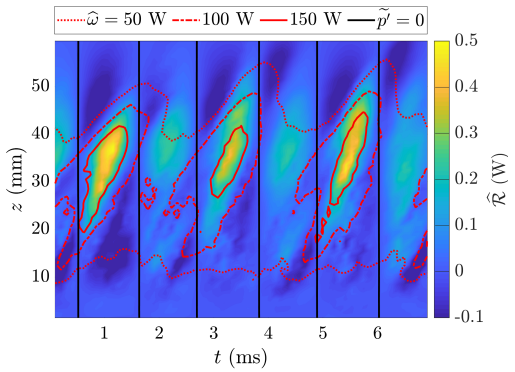

Figure 5: Space-time representation of the evolution of the Rayleigh source term $\hat{\mathcal{R}}$ during three cycles.

$$\widehat{\mathcal{R}}(z,t) = \frac{\gamma - 1}{\gamma p_0} \int_z^{z+\Delta z} \int_{S_c} p' \dot{\omega}' \, dS dz \tag{2}$$

where p' is the acoustic pressure and $\dot{\omega}'$ the heat release rate fluctuations. This term is plotted alongside isocontours of acoustic pressure (black) and locally integrated heat release rate $\widehat{\omega}$ in Fig. 5. As expected the source term is globally positive which is necessary for feeding energy into the oscillation to compensate damping. Pressure and heat release rate fluctuations are in phase. Driving is concentrated in the upper section of the flame, between $20 < z < 40\,\text{mm}$. Heat release rate perturbations exhibit a convective motion, and the delay between pressure and heat release rate perturbations corresponds to one acoustic period.

It is next interesting to examine time histories of different variables in the active region at $z = 30\,\text{mm}$ plotted in Fig. 6. Heat release rate $\widehat{\omega}$ and Rayleigh source term $\widehat{\mathcal{R}}$ are plotted in the bottom subfigure. The acoustic pressure $\widetilde{p'}$ and section averaged axial velocity $\widetilde{u_z}$ shown in the top subfigure, are in phase quadrature, as expected for a standing acoustic wave. The total mass

flow rate $\widetilde{\dot{m}_{tot}}$ and the flow rate of axial momentum $\widetilde{\mathcal{F}_z}$ appear in the second row.These two variables are in near quadrature with the axial velocity. While the axial velocity reflects the acoustic motion, the mass and momentum flow rates still feature a convective nature. The next subfigure shows the vaporization mass transfer $\widehat{\dot{m}_{vap}}$ between liquid and gas. Its fluctuations are ahead of the heat release rate. The equivalence ratio ϕ_g of the gas phase (Bilger's formulation [22]) is plotted alongside. Its values are only considered in regions where the volumetric heat release rate exceeds a threshold of 1% of its maximum. The equivalence ratio is not constant and reaches its minimum values when the heat release rate is at its maximum. The next subfigure shows the relative fluctuations of the instantaneous swirl number defined as the ratio of the axial flow rates of moment of tangential momentum $\widetilde{\mathcal{F}_\theta}$ and axial momentum $\widetilde{\mathcal{F}_z}$ [23]:

$$\widetilde{\mathcal{S}}(z,t) = \frac{\widetilde{\mathcal{F}_\theta}}{R\,\widetilde{\mathcal{F}_z}} = \frac{\int_{S_c} \rho u_z u_\theta r \, dS}{R \int_{S_c} \rho u_z^2 \, dS} \tag{3}$$

It fluctuates in phase opposition to the pressure. The same graph also shows the radial position of the barycenter of heat realease rate which oscillates in phase with the heat release rate.

It is now instructive to examine the formation and convection of these swirl number perturbations. Figure 7(a) shows the time and space evolution of $\widetilde{\mathcal{F}_z}$. Strong fluctuations are released from the injector region in near phase quadrature with pressure. They are then convected downstream. The fluctuations of heat release rate (red isocontours) are in phase with $\widetilde{\mathcal{F}_z}$ and likewise convected by the flow (Fig. 7(a) and 7(c)). The relative fluctuations of swirl number $\widetilde{\mathcal{S}}'/\overline{\mathcal{S}}$ plotted in Fig. 7(b) reach about 32 % (RMS) in the

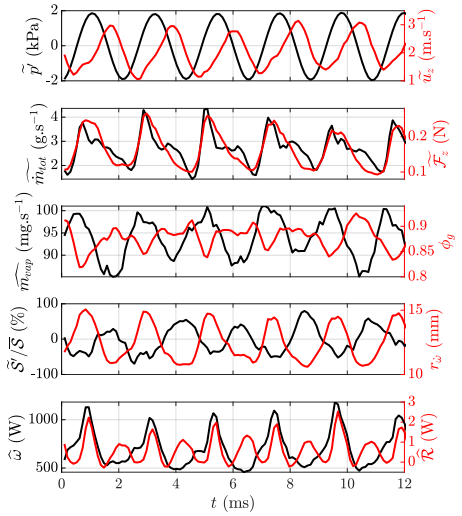

Figure 6: Temporal evolution of several flow variables integrated / averaged ($\widehat{\psi}$ or $\widetilde{\psi}$, Eq. (1)) between $z = 27.5$ and 32.5 mm (for this figure, $\Delta z = 5$ mm).

lower flame region in phase opposition with these fluxes. In the upper flame region, the swirl number fluctuations are as intense, but in phase with the heat release rate. The perturbation is initiated in the vicinity of the injector and convected downstream. Oscillations in the flame position (black and yellow isocontours) are in phase opposition with the swirl number in the lower part of the flame, which appears to dictate their position further downstream. This differs from what was found in a previous study on premixed bluff-body swirl stabilized V-flames [23], where flame opening was in phase with swirl number fluctuations at the base of the flame. Fluctuations further downstream were not examined. The phase of the different perturbations with respect to pressure is plotted as a function of the axial position in Fig. 7(c). Downstream of the injector, $\Phi_{p'}\left(\widetilde{\mathcal{F}_z}\right) = 3\pi/4$. The phase velocity of the perturbation decelerates in the first 15 mm to reach a quasi-steady value of

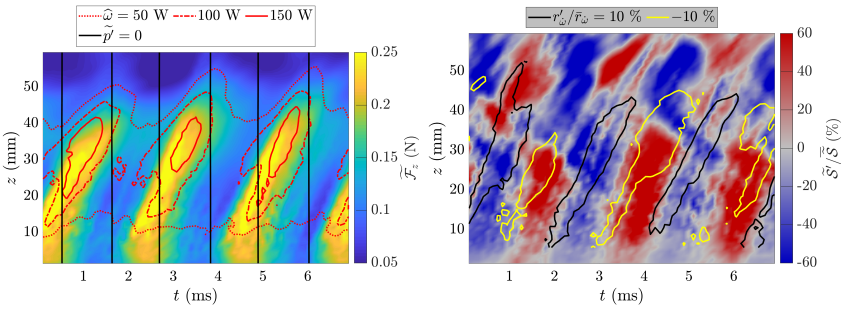

(a) Axial flux of axial momentum. (b) Swirl number fluctuations.

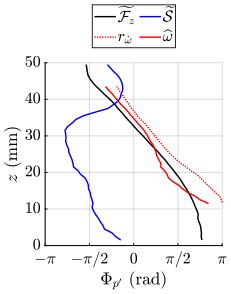

(c) Phase plot.

Figure 7: Analysis of swirl number fluctuations. **(a)** 1D-1T colormap of axial flux of axial momentum $\widetilde{\mathcal{F}_z}$ with isocontours of heat release rate $\widetilde{\omega}$ and acoustic pressure $\widetilde{p}'$. **(b)**: 1D-1T colormap of fluctuations of instantaneous swirl number $\widetilde{\mathcal{S}}$ with isocontours of heat release rate barycenter fluctuations $r'_{\dot{\omega}}/\overline{r_{\dot{\omega}}}$. **(c)** Axial evolution of the phase related to pressure for $\widetilde{\mathcal{F}_z}$, $\widetilde{\mathcal{F}_\theta}$, $\widetilde{\mathcal{S}}$, $\widehat{\omega}$ and $r_{\dot{\omega}}$.

$v_\Phi\left(\widetilde{\mathcal{F}_z}\right) = 27\,\mathrm{m\,s^{-1}}$ between $z = 20$ and $40\,\mathrm{mm}$. This corresponds to about half the cold flow jet velocity [12].

It is next interesting to examine the total mass flow rate (Fig. 8(a)). It adopts a striking behavior: its perturbations released by the injector in phase opposition to pressure are convected up to the flame region ($z \simeq 35\,\mathrm{mm}$). Further downstream its behavior is dominated by acoustics with vertical alternating bands characteristic of velocity fluctuations in quadrature with

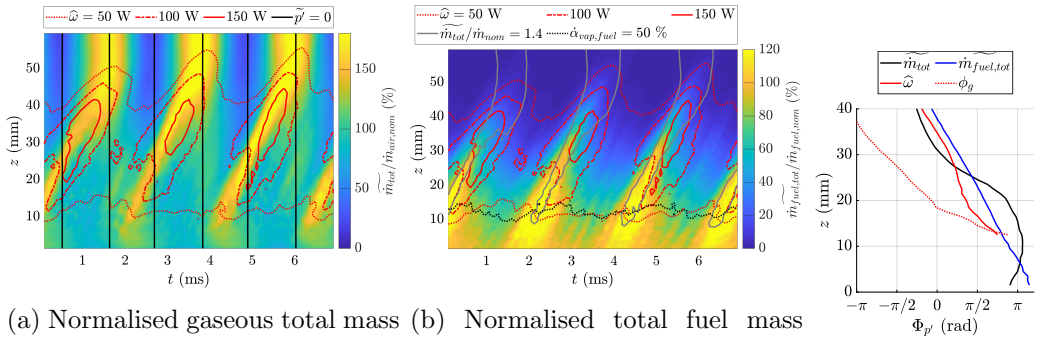

(a) Normalised gaseous total mass flow rate.

(b) Normalised total fuel mass flow rate.

(c) Phase plot.

Figure 8: Analysis of mass flow convective patterns. **(a)** 1D-1T colormap of total mass flow rate $\widetilde{\dot{m}_{tot}}$ normalized by the nominal air mass flow rate. Isocontours of heat release rate $\widehat{\omega}$ and acoustic pressure $\widetilde{p'}$. **(b)**: 1D-1T colormap of total fuel mass flow rate $\widetilde{\dot{m}_{fuel,tot}}$ normalized by the nominal fuel flow rate. Isocontours of integrated heat release rate $\widehat{\omega}$, total mass flux $\widetilde{\dot{m}_{tot}}$ and fuel flow rate vapor fraction $\dot{\alpha}_{vap,fuel}$. **(c)** Axial evolution of the phase with respect to pressure for $\widetilde{\dot{m}_{tot}}$, $\widetilde{\dot{m}_{fuel,tot}}$, $\widehat{\omega}$ and ϕ_g.

pressure of the quarter wave mode. Figure 8(b) displays the total fuel flow rate. Although the injected fuel flow rate in the atomizer is constant, the dynamics of the injector creates 10 % (RMS) fluctuations in the fuel flow rate at the outlet of the injector, in a process most likely similar to that presented in [2] and further discussed in [21]. The phase to acoustic pressure is $\Phi_{p'}\left(\widetilde{\dot{m}_{fuel,tot.}}\right) = -7\pi/8$. This perturbation is convected at $v_\Phi\left(\widetilde{\dot{m}_{fuel,tot.}}\right) \simeq 28\,\mathrm{m\,s^{-1}}$, essentially the same phase velocity as the swirl number fluctuations. The phase plots in Fig. 8(c) complement the heat release rate isocontours in Fig. 8(a) and 8(b). There is a time delay between the fuel flow perturbation and the heat release rate which varies as a function of the axial position. One finds for example that $\tau_{ch}(z = 20\,\mathrm{mm}) = 0.25\,\mathrm{ms}$ and $\tau_{ch}(z = 30\,\mathrm{mm}) = 0.12\,\mathrm{ms}$. These values are typical of combustion delays under similar conditions [3].

This analysis now allows to estimate the various delays in the process. This can be decomposed into three contributions: firstly, the response of the injector which produces aerodynamic disturbances and flowrate fluctuations with a delay $\tau_{inj} = 0.95\,\mathrm{ms}$. Secondly, the perturbation is convected at a phase velocity $v_\Phi \simeq 28\,\mathrm{m\,s^{-1}}$ to the flame zone, located approximately 35 mm downstream in the high Rayleigh source term region (Fig. 5). This corresponds to a second delay $\tau_{cv} = 1.25\,\mathrm{ms}$. Thirdly, the combustion delay discussed previously must be accounted for. The total delay

$$\tau_t = \tau_{inj} + \tau_{cv} + \tau_{ch} \simeq 2.32\,\mathrm{ms} \tag{4}$$

is approximately equal to the delay between pressure fluctuations acting on the injector and heat release rate fluctuation which is about equal to the acoustic period 2.17 ms. Surprisingly the vaporization delay does not contribute to the total delay. This is because vaporization occurs simultaneously with convection. This is confirmed in Fig. 8(b) where the black dotted isocontour shows the region downstream of which more than 50 % of the fuel flow rate is being convected in gaseous form: $\dot{\alpha}_{vap,fuel} = \widetilde{\dot{m}_{fuel,vap}}/\widetilde{\dot{m}_{fuel,tot}}$. This contour is around $z = 12\,\mathrm{mm}$. This also substantiates what was inferred in [3] for a lean premixed prevaporized injector.

5. Conclusion

Large Eddy Simulation (LES) and experiments are combined to analyze acoustically coupled combustion oscillations in a generic configuration equipped with a swirling spray injector. The calculations essentially retrieve the frequency and amplitude of oscillation and are in fair agreement with

the observed flame and spray dynamics. Comparisons of the flame and spray dynamics are performed using identical post-processing of experimental and numerical data, making use of the dynamic mode decomposition to analyze the oscillations. The data produced by the simulation is then processed to extract the mechanisms responsible for the intertwined response of the flame and the spray to the acoustic perturbation. This is done by noting that the flame is compact with respect to the acoustic wavelength and by making use of variables integrated over the combustor cross section. This gives access to the space time representation of central variables that are not easily measured experimentally and from which one observes that : (1) Sizable swirl number fluctuations are generated by the acoustic motion and convected by the jet. They have a strong impact on the aerodynamics of the flow and induce radial oscillations in the flame location. (2) Fluctuations of fuel flow rate are initiated in phase opposition to these swirl number fluctuations and likewise convected. (3) The total mass flow rate features a peculiar behavior: from the chamber backplane to the end of the combustion region it presents a convective motion while further downstream its fluctuations are dominated by the acoustic motion. These various mechanisms contribute to the shaping of the heat release perturbations and the associated delay with respect to the pressure. This delay combines the response time of the injector to pressure disturbances, the convection time to the flame zone and the chemical conversion characteristic time while the vaporization time needs not to be included because it takes place simultaneously with convection.

Acknowledgments

Support is provided by France's ANR (FASMIC ANR16-CE22-0013), the EU H2020 MSCA-ITN ANNULIGHT (No 765998) and MSCA-IF CLEAN-ERFLAMES (No 843958), SafranTech (NF5Z-5100), Mésocentre Centrale-Supélec/ENS Paris-Saclay and GENCI-CINES for HPC ressources (2020-A0052B10157).

References

[1] W. Konrad, N. Brehm, F. Kameier, C. Freeman, I. J. Day, Combustion Instability Investigations on the BR710 Jet Engine, J. Eng. Gas Turb. Power 120 (1) (1998) 34–40.

[2] J. Eckstein, E. Freitag, C. Hirsch, T. Sattelmayer, Experimental study on the role of entropy waves in low-frequency oscillations in a RQL combustor, J. Eng. Gas Turb. Power 128 (2) (2006) 264–270.

[3] D. Bernier, F. Lacas, S. Candel, Instability mechanisms in a premixed prevaporized combustor, J. Propul. Power 20 (4) (2004) 648–656.

[4] M. de la Cruz García, E. Mastorakos, A. P. Dowling, Investigations on the self-excited oscillations in a kerosene spray flame, Combust. Flame 156 (2) (2009) 374–384.

[5] Y. Huang, V. Yang, Dynamics and stability of lean-premixed swirl-stabilized combustion, Prog. Energ. Combust. 35 (4) (2009) 293–364.

[6] S. Tachibana, K. Saito, T. Yamamoto, M. Makida, T. Kitano, R. Kurose, Experimental and numerical investigation of thermo-acoustic instability

in a liquid-fuel aero-engine combustor at elevated pressure: Validity of large-eddy simulation of spray combustion, Combust. Flame 162 (6) (2015) 2621–2637.

[7] M. Zhu, A. P. Dowling, K. N. Bray, Transfer function calculations for aeroengine combustion oscillations, J. Eng. Gas Turb. Power 127 (1) (2005) 18–26.

[8] A. Innocenti, A. Andreini, B. Facchini, A. Peschiulli, Numerical analysis of the dynamic flame response of a spray flame for aero-engine applications, Int. J. Spray Combust. Dynam. 9 (4) (2017) 310–329.

[9] W. P. Jones, A. J. Marquis, K. Vogiatzaki, Large-eddy simulation of spray combustion in a gas turbine combustor, Combust. Flame 161 (1) (2014) 222–239.

[10] F. Shum-Kivan, J. Marrero Santiago, A. Verdier, E. Riber, B. Renou, G. Cabot, B. Cuenot, Experimental and numerical analysis of a turbulent spray flame structure, Proc. Combust. Inst. 36 (2) (2017) 2567–2575.

[11] T. Kitano, K. Kaneko, R. Kurose, S. Komori, Large-eddy simulations of gas- and liquid-fueled combustion instabilities in back-step flows, Combust. Flame 170 (2016) 63–78.

[12] K. Prieur, D. Durox, T. Schuller, S. Candel, Strong Azimuthal Combustion Instabilities in a Spray Annular Chamber With Intermittent Partial Blow-Off, J. Eng. Gas Turb. Power 140 (3) (2017) 031503.

[13] L. Crocco, S.-I. Cheng, Theory of combustion instability in liquid propellant rocket motors, in: NATO (Ed.), Agardograph 8, Butterworth Scientific Publication, 1956.

[14] K. Prieur, D. Durox, J. Beaunier, T. Schuller, S. Candel, Ignition dynamics in an annular combustor for liquid spray and premixed gaseous injection, Proc. Combust. Inst. 36 (3) (2017) 3717–3724.

[15] F. Nicoud, H. B. Toda, O. Cabrit, S. Bose, J. Lee, Using singular values to build a subgridscale model for large eddy simulations, Phys. Fluids 23 (8).

[16] G. Chaussonnet, O. Vermorel, E. Riber, B. Cuenot, A new phenomenological model to predict drop size distribution in large-eddy simulations of airblast atomizers, Int. J. Multiph. Flow 80 (2016) 29–42.

[17] J. Urzay, M. Bassenne, G. I. Park, P. Moin, Characteristic regimes of subgrid-scale coupling in LES of particle-laden turbulent flows, in: Annu. Res. Briefs: Cent. Turbul. Res., 2014.

[18] D. Paulhiac, Modélisation de la combustion d'un spray dans un brûleur aéronautique, Ph.D. thesis, INPT (2015).

[19] P. J. Schmid, Dynamic mode decomposition of numerical and experimental data, J. Fluid Mech. 656 (2010) 5–28.

[20] D. Durox, T. Schuller, N. Noiray, S. Candel, Experimental analysis of nonlinear flame transfer functions for different flame geometries, Proc. Combust. Inst. 32 (1) (2009) 1391–1398.

[21] E. Lo Schiavo, D. Laera, E. Riber, L. Gicquel, T. Poinsot, Effect of liquid fuel wall interaction on thermoacoustic instabilities in swirling spray flames, Combust. Flame, accepted.

[22] R. Bilger, S. Stårner, R. Kee, On reduced mechanisms for methane air combustion in nonpremixed flames, Combust. Flame 80 (2) (1990) 135–149.

[23] P. Palies, D. Durox, T. Schuller, S. Candel, The combined dynamics of swirler and turbulent premixed swirling flames, Combust. Flame 157 (9) (2010) 1698–1717.